PERGAMON

International Journal of Heat and Mass Transfer 45 (2002) 3071–3087

International Journal of HEAT and MASS TRANSFER

www.elsevier.com/locate/ijhmt

Constant wall heat flux boundary conditions in porous media under local thermal non-equilibrium conditions

Bader Alazmi [a], Kambiz Vafai [b,*]

[a] Department of Mechanical Engineering, The Ohio State University, 206 West 18th Avenue, Columbus, OH 43210-1107, USA
[b] Department of Mechanical Engineering, University of California, A363 Bourns Hall, Riverside, CA 92521-0425, USA

Received 10 October 2001; received in revised form 8 January 2002

Abstract

Boundary conditions for constant wall heat flux in the absence of local thermal equilibrium conditions are analyzed in this work. Effects of variable porosity and thermal dispersion are also analyzed. Different forms of constant heat flux boundary conditions found in the literature were investigated in this work. The effects of pertinent parameters such as porosity, Darcy number, Reynolds number, inertia parameter, particle diameter and solid-to-fluid conductivity ratio were analyzed. Quantitative and qualitative interpretations of the results are utilized to investigate the prominent characteristics of the models under consideration. Limiting cases resulting convergence or divergence of the models are also considered. Results are presented in terms of the fluid, solid and total Nusselt numbers.

1. Introduction

In recent years, the problem of local thermal non-equilibrium (LTNE) has received considerable attention due to its relevance in a wide variety of engineering applications such as electronic cooling, heat pipes, nuclear reactors, drying technology, multiphase catalytic reactors and others. The use of two-equation model is required for these types of problems. Each energy equation, one for the fluid phase and the other for the solid phase, requires a boundary condition at the solid boundary. Hitherto, it is not clear what two boundary conditions might be used for the case of constant wall heat flux. In contrast, boundary conditions for constant wall temperature are clear, both phases should have a temperature that equals a prescribed wall temperature.

The study of Amiri et al. [1] was one of the first attempts to highlight this problem and present two different approaches for boundary conditions for constant wall heat flux. The first approach presented in their work was based on assuming the total heat flux q_w being divided between the two phases depending on the physical values of their effective conductivities and their corresponding temperature gradients at the wall. The second approach also presented in Amiri et al. [1] assumes that each of the individual phases at the wall receives an equal amount of the total heat flux q_w. In their study, good agreements were found between the numerical results using the second approach and the available experimental results. On the other hand, Hwang et al. [2] used the first approach and found good agreement between their numerical and experimental results. Lee and Vafai [3] used the first approach to obtain analytical solutions for the temperature profiles, the temperature difference between the two phases, and the Nusselt number. Several other studies [4–9] considered the first approach to investigate the problem of LTNE in porous media. Martin et al. [10] used the first approach with the assumption of local thermal equilibrium at the wall. That is the temperature gradients for both phases were taken to be the same in their work. Jiang and Ren [11] considered four boundary conditions for the case of

* Corresponding author. Tel.: +1-909-787-2135; fax: +1-909-787-2899.
E-mail address: vafai@engr.ucr.edu (K. Vafai).

0017-9310/02/$ - see front matter
PII: S0017-9310(02)00044-3

Nomenclature

a_{sf}	specific surface area (m^{-1})
b	porosity variation parameter defined in Eq. (11)
c	porosity variation parameter defined in Eq. (11)
c_p	specific heat at constant pressure (J kg^{-1} K^{-1})
d_p	particle diameter (m)
Da	Darcy number, K/H^2
F	geometric function defined in Eq. (13)
H	height of the channel (m)
h_{sf}	fluid-to-solid heat transfer coefficient (W m^{-2} K^{-1})
J	unit vector aligned along the pore velocity
k	thermal conductivity (W m^{-1} K^{-1})
K	permeability (m^2)
L	channel length (m)
Nu	local Nusselt number
$\overline{Nu}$	average Nusselt number
P	pressure ($N m^{-2}$)
Pr	Prandtl number (ν/α)
Re_p	particle Reynolds number, $u_\infty d_P/\nu_f$
T	temperature (K)
T_m	mean temperature (K)
u	velocity in x-direction (m s^{-1})
u_c	convective velocity in x-direction (m s^{-1})
U	non-dimensional velocity, u/u_∞
U_m	mean velocity
V	velocity vector (m s^{-1})
x, y	Cartesian coordinates (m)
Y	non-dimensional coordinate, y/H

Greek symbols

α	thermal diffusivity (m^2 s^{-1})
ε	porosity
κ	solid-to-fluid thermal conductivity ratio, k_s/k_f
Λ	inertia parameter, $\varepsilon^{3/2} F u_c H/\nu$
μ	dynamic viscosity (kg m^{-1} s^{-1})
ν	kinematic viscosity (m^2 s^{-1})
ρ	density (kg m^{-3})
ξ	dimensionless axial length scale, x/L.

Subscripts

eff	effective property
f	fluid
s	solid
t	total
w	wall
∞	free stream

Other symbol

$\langle\rangle$	'local volume average' of a quantity

constant heat flux. These were composed of the two approaches presented by Amiri et al. [1], the model presented by Martin et al. [10], and a fourth model which can be considered as a very special case of the first approach. They reported that using the second approach corresponds well to the experimental results of Jiang et al. [12]. Correspondingly, the second approach was employed in other studies [13–16] to study the problem of thermal non-equilibrium.

The main objective of the present study is to analyze the effect of using different boundary conditions for the case of constant wall heat flux under LTNE conditions. In addition to the above-mentioned boundary conditions, five pertinent new boundary conditions are introduced in the present study. Pertinent parameters such as porosity, Reynolds number, Darcy number, inertia parameter, particle diameter, and solid-to-fluid conductivity ratio are considered to assess and compare the physical features of different boundary conditions under investigation.

2. Analysis

A fundamental unit for analyzing this problem is selected. As such a parallel plate channel subject to an imposed constant heat flux is considered to analyze the proper set of boundary conditions in porous media under LTNE conditions. Fig. 1 shows the schematic diagram of the problem under consideration. The steady-state volume averaged governing equations [1,17] are

Continuity

$$\nabla\langle V\rangle = 0. \tag{1}$$

Momentum

$$\frac{\rho_f}{\varepsilon}\langle (V\nabla)V\rangle = -\frac{\mu_f}{K}\langle V\rangle - \frac{\rho_f F\varepsilon}{\sqrt{K}}(\langle V\rangle\langle V\rangle)J + \frac{\mu_f}{\varepsilon}\nabla^2\langle V\rangle - \nabla\langle P\rangle^f. \tag{2}$$

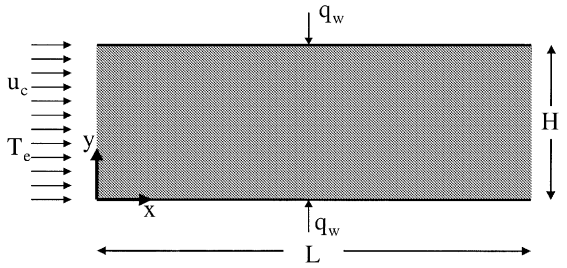

Fig. 1. Schematic diagram of the problem of constant wall heat flux boundary conditions in porous media under LTNE conditions and the corresponding coordinate system.

Fluid phase energy

$$\langle \rho_f \rangle^f C_{p_f} \langle V \rangle \nabla \langle T_f \rangle^f = \nabla \left(k_{f_{eff}} \nabla \langle T_f \rangle^f \right) + h_{sf} a_{sf} \left(\langle T_s \rangle^s - \langle T_f \rangle^f \right). \tag{3}$$

Solid phase energy

$$0 = \nabla \left(k_{s_{eff}} \nabla \langle T_s \rangle^s \right) - h_{sf} a_{sf} \left(\langle T_s \rangle^s - \langle T_f \rangle^f \right). \tag{4}$$

The fluid-to-solid heat transfer coefficient is expressed as [1,17]

$$h_{sf} = \frac{k_f}{d_p} \left[2 + 1.1 Pr^{1/3} \left(\frac{\rho_f u d_p}{\mu_f} \right)^{0.6} \right]. \tag{5}$$

While the specific surface area of the bed can be expressed as

$$a_{sf} = \frac{6(1-\varepsilon)}{d_p}. \tag{6}$$

Effective conductivities of both phases are defined as

$$k_{f_{eff}} = \varepsilon k_f, \tag{7}$$

$$k_{s_{eff}} = (1-\varepsilon) k_s. \tag{8}$$

In some cases, it is important to account for the effects of variable porosity and thermal dispersion. Effective conductivities of the fluid phase can be represented as [17]

$$(k_{f_{eff}})_x = \left[\varepsilon + 0.5 Pr \left(\frac{\rho_f u d_p}{\mu} \right) \right] k_f, \tag{9}$$

$$(k_{f_{eff}})_y = \left[\varepsilon + 0.1 Pr \left(\frac{\rho_f u d_p}{\mu} \right) \right] k_f \tag{10}$$

and variable porosity can be expressed as [17,18]

$$\varepsilon = \varepsilon_\infty \left[1 + b \exp \left(\frac{-cy}{d_p} \right) \right]. \tag{11}$$

Furthermore, permeability and the geometric function F are expressed as [17,18]

$$K = \frac{\varepsilon^3 d_p^2}{150(1-\varepsilon)^2}, \tag{12}$$

$$F = \frac{1.75}{\sqrt{150 \varepsilon^3}}. \tag{13}$$

Local Nusselt numbers for both phases are defined according to [17] as

$$Nu_{\mathrm{f}} = -\frac{2H}{\langle T_{\mathrm{f}}\rangle^{\mathrm{f}}_{\mathrm{w}} - \langle T_{\mathrm{f}}\rangle^{\mathrm{f}}_{\mathrm{m}}}\left(\frac{\partial\langle T_{\mathrm{f}}\rangle^{\mathrm{f}}}{\partial y}\right)_{y=0}, \tag{14}$$

$$Nu_{\mathrm{s}} = -\frac{2H}{\langle T_{\mathrm{s}}\rangle^{\mathrm{s}}_{\mathrm{w}} - \langle T_{\mathrm{s}}\rangle^{\mathrm{s}}_{\mathrm{m}}}\left(\frac{\partial\langle T_{\mathrm{s}}\rangle^{\mathrm{s}}}{\partial y}\right)_{y=0}, \tag{15}$$

where the mean temperatures $\langle T_{\mathrm{f}}\rangle^{\mathrm{f}}_{\mathrm{m}}$ and $\langle T_{\mathrm{s}}\rangle^{\mathrm{s}}_{\mathrm{m}}$ are defined as

$$\langle T_{\mathrm{f}}\rangle^{\mathrm{f}}_{\mathrm{m}} = \frac{1}{U_{\mathrm{m}}H}\int_0^H u\langle T_{\mathrm{f}}\rangle^{\mathrm{f}}\,\mathrm{d}y, \tag{16}$$

$$\langle T_{\mathrm{s}}\rangle^{\mathrm{s}}_{\mathrm{m}} = \frac{1}{H}\int_0^H \langle T_{\mathrm{s}}\rangle^{\mathrm{s}}\,\mathrm{d}y, \tag{17}$$

where

$$U_{\mathrm{m}} = \frac{1}{H}\int_0^H u\,\mathrm{d}y. \tag{18}$$

The average Nusselt numbers ($\overline{Nu}_{\mathrm{f}}$ and $\overline{Nu}_{\mathrm{s}}$) over the length of the bed are expressed as

$$\overline{Nu}_{\mathrm{f}} = \frac{1}{L}\int_0^L Nu_{\mathrm{f}}\,\mathrm{d}x, \tag{19}$$

$$\overline{Nu}_{\mathrm{s}} = \frac{1}{L}\int_0^L Nu_{\mathrm{s}}\,\mathrm{d}x. \tag{20}$$

Consequently, the total Nusselt number ($\overline{Nu}_{\mathrm{t}}$) is defined as the summation of $\overline{Nu}_{\mathrm{f}}$ and $\overline{Nu}_{\mathrm{s}}$:

$$\overline{Nu}_{\mathrm{t}} = \overline{Nu}_{\mathrm{f}} + \overline{Nu}_{\mathrm{s}}. \tag{21}$$

Table 1
Summary of different models based on the two approaches and the corresponding references

Approach	Model	Mathematical representation	References
First	1A	$q_{\mathrm{w}} = -k_{\mathrm{f_{eff}}}\left.\frac{\partial T_{\mathrm{f}}}{\partial y}\right\|_{\mathrm{wall}} - k_{\mathrm{s_{eff}}}\left.\frac{\partial T_{\mathrm{s}}}{\partial y}\right\|_{\mathrm{wall}} \quad T_{\mathrm{f_w}} = T_{\mathrm{s_w}} = T_{\mathrm{w}}$	[1–8,10]
	1B	$q_{\mathrm{w}} = -[\varepsilon k_{\mathrm{f}} + (1-\varepsilon)k_{\mathrm{s}}]\left.\frac{\partial T_{\mathrm{f}}}{\partial y}\right\|_{\mathrm{wall}} \quad T_{\mathrm{f_w}} = T_{\mathrm{s_w}} = T_{\mathrm{w}}$	[9,10]
	1C	$q_{\mathrm{w}} = -[\varepsilon k_{\mathrm{f}} + (1-\varepsilon)k_{\mathrm{s}}]\left.\frac{\partial T_{\mathrm{s}}}{\partial y}\right\|_{\mathrm{wall}} \quad T_{\mathrm{f_w}} = T_{\mathrm{s_w}} = T_{\mathrm{w}}$	Present Study
	1D[a]	$q_{\mathrm{w}} = -k_{\mathrm{f_{eff}}}\left.\frac{\partial T_{\mathrm{f}}}{\partial y}\right\|_{\mathrm{wall}} - k_{\mathrm{s_{eff}}}\left.\frac{\partial T_{\mathrm{s}}}{\partial y}\right\|_{\mathrm{wall}} \quad \frac{q_{\mathrm{f}}}{q_{\mathrm{s}}} = \frac{\varepsilon}{1-\varepsilon}$	Present Study
	1E	$q_{\mathrm{w}} = -k_{\mathrm{f_{eff}}}\left.\frac{\partial T_{\mathrm{f}}}{\partial y}\right\|_{\mathrm{wall}} - k_{\mathrm{s_{eff}}}\left.\frac{\partial T_{\mathrm{s}}}{\partial y}\right\|_{\mathrm{wall}} \quad \frac{q_{\mathrm{f}}}{q_{\mathrm{s}}} = \frac{k_{\mathrm{f}}}{k_{\mathrm{s}}}$	Present Study
	1F[a]	$q_{\mathrm{w}} = -k_{\mathrm{f_{eff}}}\left.\frac{\partial T_{\mathrm{f}}}{\partial y}\right\|_{\mathrm{wall}} - k_{\mathrm{s_{eff}}}\left.\frac{\partial T_{\mathrm{s}}}{\partial y}\right\|_{\mathrm{wall}} \quad \frac{q_{\mathrm{f}}}{q_{\mathrm{s}}} = \frac{\varepsilon k_{\mathrm{f}}}{(1-\varepsilon)k_{\mathrm{s}}}$	Present Study
Second	2A	$q_{\mathrm{w}} = -k_{\mathrm{f_{eff}}}\left.\frac{\partial T_{\mathrm{f}}}{\partial y}\right\|_{\mathrm{wall}} = -k_{\mathrm{s_{eff}}}\left.\frac{\partial T_{\mathrm{s}}}{\partial y}\right\|_{\mathrm{wall}}$	[1]
	2B	$q_{\mathrm{w}} = -k_{\mathrm{f}}\left.\frac{\partial T_{\mathrm{f}}}{\partial y}\right\|_{\mathrm{wall}} = -k_{\mathrm{s}}\left.\frac{\partial T_{\mathrm{s}}}{\partial y}\right\|_{\mathrm{wall}}$	[10–13]

[a] Free stream porosity 'ε_∞' is used when the effect of variable porosity is considered.

Mathematical representations of the pertinent boundary conditions for the case of constant heat flux are shown in Table 1. Six models (1A, 1B, 1C, 1D, 1E and 1F) are based on the first approach and two models (2A and 2B) are based on the second approach presented in [1].

3. Numerical methodology

The governing equations were solved numerically using the finite difference method. No-slip boundary conditions at the wall were employed for the momentum equation while appropriate boundary conditions from Table 1 were used for the energy equations. The momentum equation was solved by a tridiagonal scheme after linearizing the Forchheimer term. Since the energy equations were coupled, an implicit iterative method was used to solve the temperature fields. Central differencing was used for the diffusion terms while upwind differencing was used for the convective terms. The convergence criterion was satisfied when the absolute difference between two consecutive iterations was less than 10^{-6}. Variable grids in the y-direction and uniform grids in the x-direction were employed in the present study.

4. Results and discussion

Comparison between the numerical result for the velocity and the exact solution given in Vafai and Kim [19] is shown in Fig. 2(a). Since there is no analytical solution of the LTNE that counts for the effects of axial conduction, variable porosity, and thermal dispersion, the current results are compared with the numerical results of Amiri and Vafai [17]. Excellent agreement was found between the present results and the results presented in Amiri and Vafai [17] as shown in Fig. 2(b).

Table 1 displays the detailed mathematical representation of the boundary conditions for the case of constant wall heat flux. Models 1A and 2A are the conventional boundary conditions presented by Amiri et al. [1]. Model 1A indicates that q_w is divided between the two phases on the basis of their effective thermal conductivities and their corresponding temperature gradients. Model 2A suggests that each individual phase receive exactly the same amount of the heat flux q_w. These two approaches are broad and other models can be considered as extensions of them. Models 1B and 2B were used in previous studies [9–13]. In model 1B, the total heat flux q_w is assumed to have the same representation as the case of local thermal equilibrium. In other words, it is assumed that both phases have the same temperature and temperature gradient at the wall. As mentioned above, the present problem requires only two boundary conditions at the wall. However, having the same temperature and temperature gradient at the wall in addition to the constant heat flux boundary condition provides three boundary conditions, this leads to an over specified problem. As such, the fluid phase temperature gradient of model 1B is chosen to represent the heat flux at the solid boundary and model 1C is introduced to investigate the effect of using the solid phase temperature gradient instead of the fluid phase temperature gradient, as in model 1B, in the expression of the wall heat flux.

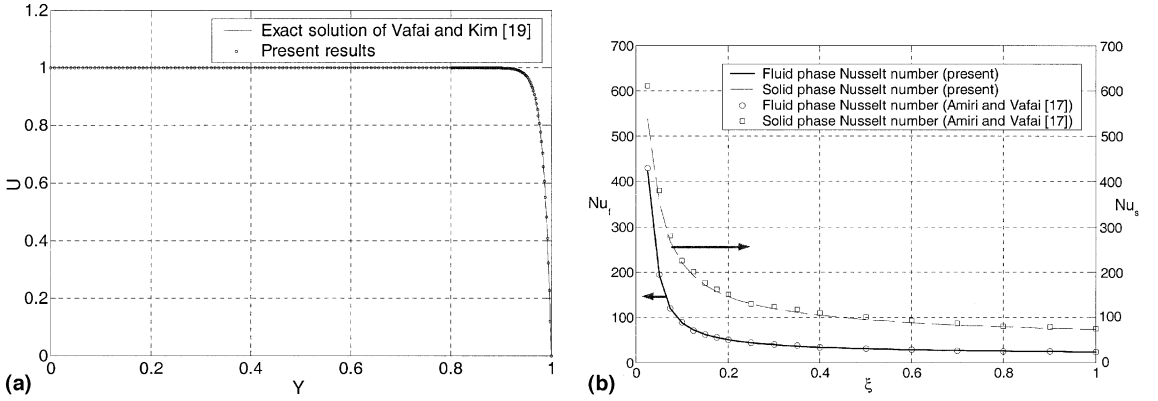

Fig. 2. Validation of the present work. (a) Comparison of the velocity profiles with the analytical solution of Vafai and Kim [19]. $Da = 10^{-3}$, $\Lambda = 70.372$, $Re_p = 200$. (b) Local Nusselt numbers of the present study against the results of Amiri and Vafai [17], $\alpha_s/\alpha_f = 25.6$, $Da = 1.36 \times 10^{-6}$ and $Re_p = 100$.

The generic models (1D, 1E and 1F) are extensions of the first approach, they are introduced for the first time in the present study. Model 1D suggests that the ratio of the fluid phase heat flux to the solid phase heat flux (q_f/q_s) depend on the porosity of the porous medium. More precisely, it is assumed that the ratio q_f/q_s is proportional to the ratio $\varepsilon/(1-\varepsilon)$. Model 1E states that the ratio q_f/q_s is proportional to the fluid-to-solid conductivity ratio κ. As shown in Table 1, model 1F is a combination of the previous two models. Finally, model 2B advocates the second approach and states that the heat flux of each phase is equal to the thermal conductivity of each phase multiplied by the temperature gradient. When the thermal conductivities of both phases are constants (thermal dispersion effects are excluded), model 2B becomes identical to model 1D. This example explains the probable equivalence between the models listed in Table 1. Therefore, an extensive investigation is performed in the present study to clarify the differences and/or the similarities between the eight models. Effects of porosity, Darcy number, Reynolds number, inertia parameter, particle diameter, and the solid-to-fluid conductivity ratio are presented. Physical properties and configuration are chosen to be similar to the ones in [1]. Results for the simplified case where the porosity is considered constant and effects of thermal dispersion are excluded are presented in Figs. 3–10. Results of the generalized model that accounts for the effects of variable porosity and thermal dispersion are demonstrated in Figs. 11–14.

4.1. Constant porosity, no thermal dispersion

It is clear that all the boundary conditions shown in Table 1 depend on the porosity, the thermal conductivities, and the temperature gradients. An important aspect of the present work is the comparison of these different models when the porosity is constant and the thermal dispersion effect is excluded. Table 2 shows the mathematical representation for q_w for each model for the special cases of $\varepsilon = 0.5$ or $\kappa = 1$, and the combination of $\varepsilon = 0.5$ and $\kappa = 1$. As shown in Table 2, it is found that models 1D, 1F, and 2B are the same when the solid-to-fluid conductivity ratio has a value of unity. When the porosity has a value of 0.5, models 1E and 1F become identical. When the two mentioned effects are combined ($\varepsilon = 0.5$ and $\kappa = 1$), models 1D, 1E, 1F, and 2B become identical. Models 1A, 1B, and 1C become identical

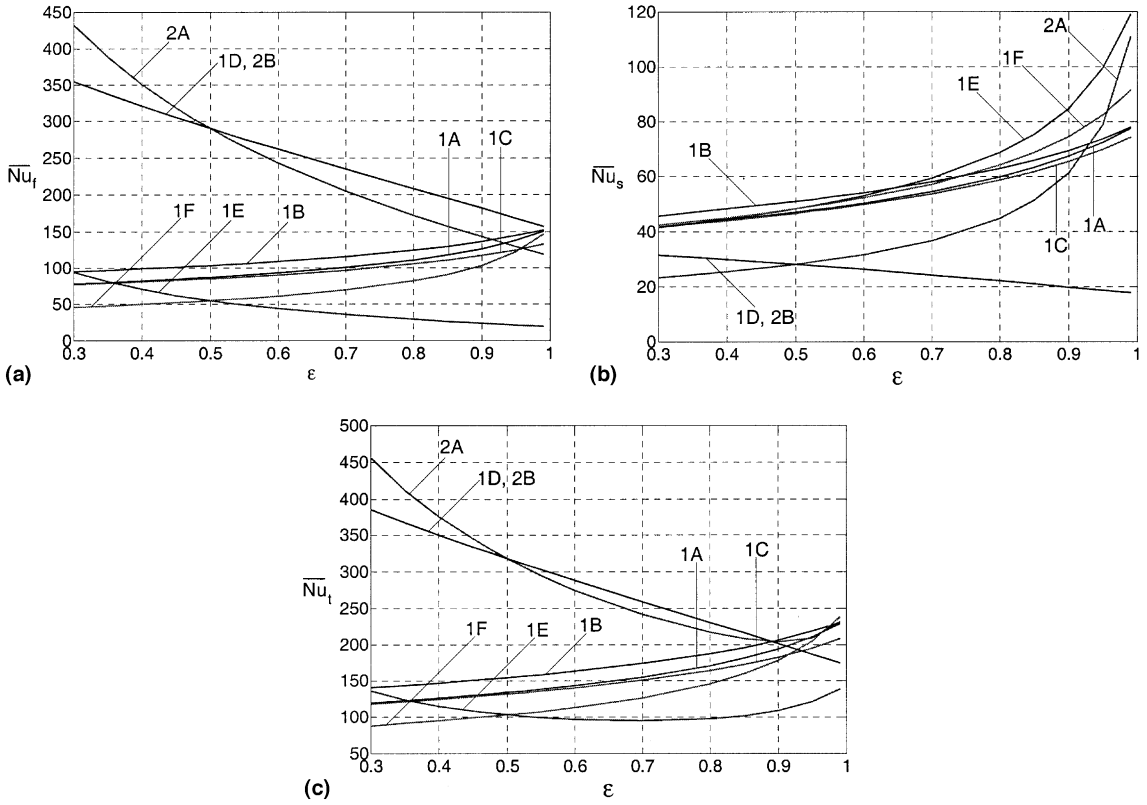

Fig. 3. Effect of porosity "ε" on the Nusselt number excluding the effects of variable porosity and thermal dispersion. $Re_p = 100$, $Da = 10^{-5}$, $\Lambda = 10$, $d_p = 0.008$, $\kappa = 23.75$. (a) Fluid phase. (b) Solid phase. (c) Total Nusselt number.

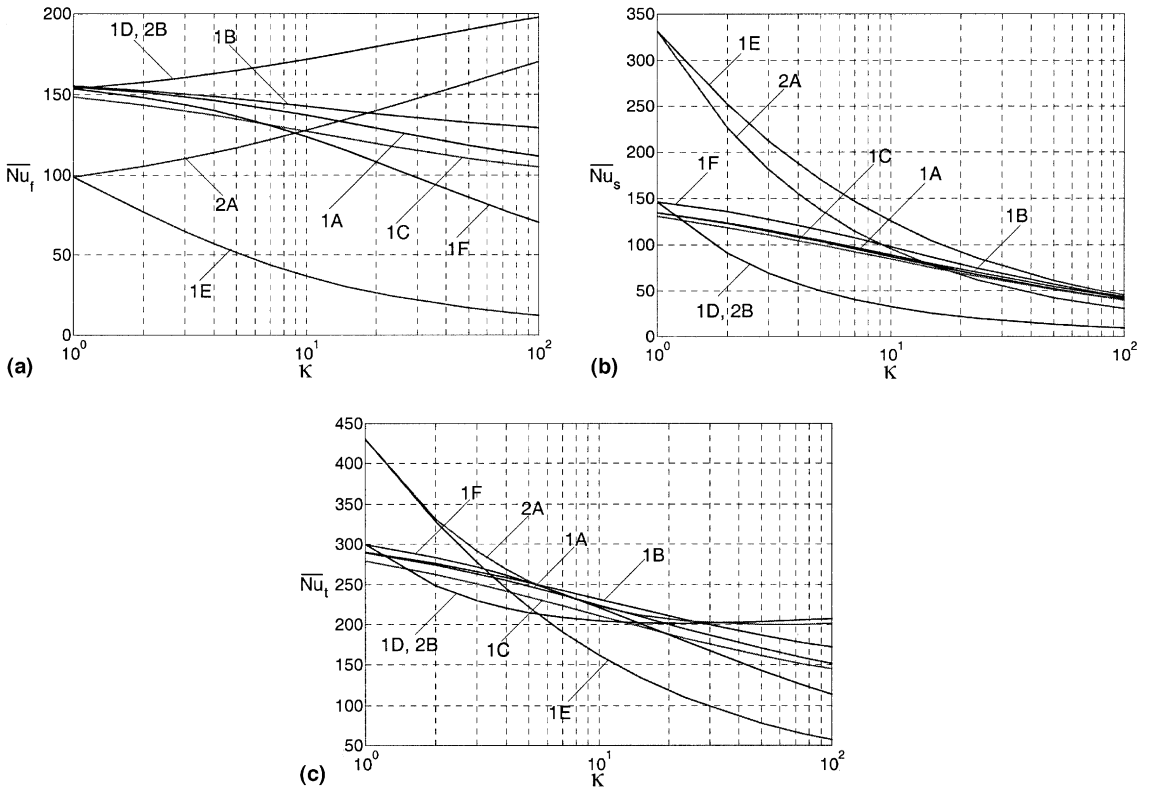

Fig. 4. Effect of the solid-to-fluid conductivity ratio "$\kappa = k_s/k_f$" on the Nusselt number excluding the effects of variable porosity and thermal dispersion. $\varepsilon = 0.9$, $Re_p = 100$, $Da = 10^{-5}$, $\Lambda = 10$, $d_p = 0.008$. (a) Fluid phase. (b) Solid phase. (c) Total Nusselt number.

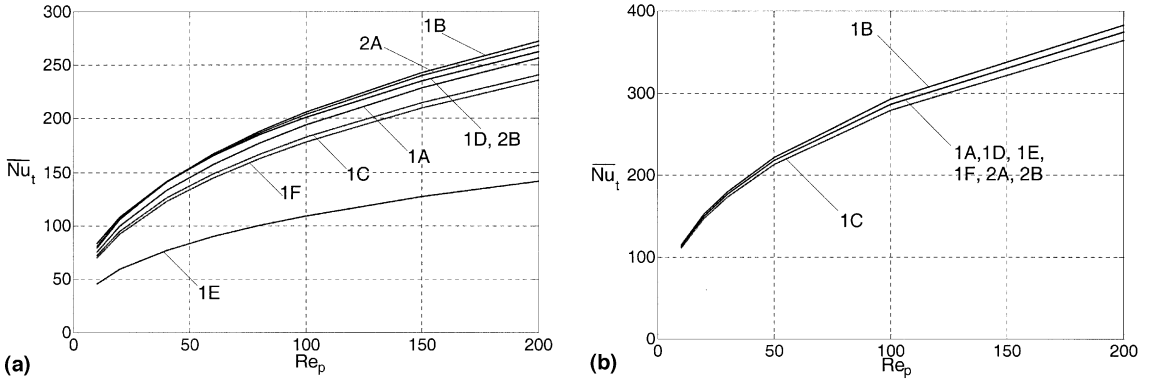

Fig. 5. Effect of particle Reynolds number "Re_p" on the total Nusselt number excluding the effects of variable porosity and thermal dispersion. (a) $\varepsilon = 0.9$, $Da = 10^{-5}$, $\Lambda = 10$, $d_p = 0.008$, $\kappa = 23.75$. (b) $\varepsilon = 0.5$, $Da = 10^{-5}$, $\Lambda = 10$, $d_p = 0.008$, $\kappa = 1.0$.

when the fluid and solid temperature gradients are the same, which happens in case of thermal equilibrium at the wall. In general, all the models converge to the same limit when the case ($\varepsilon = 0.5$ and $\kappa = 1$) is satisfied. It is clear from Tables 1 and 2 that model 1A always falls between models 1B and 1C. In fact, when models 1B and 1C give the same results, it means that there is a thermal equilibrium at the wall. In other words, models 1B and 1C do not become identical unless the temperature gradients of both phases are the same at the solid boundary. It is important to note that temperature gradients of model 2A for the special case of ($\varepsilon = 0.5$ and $\kappa = 1$) are almost twice the ones for the other models.

For simplicity, model 1D will not be mentioned in this discussion since it becomes identical to model 2B. Effect of the porosity is illustrated in Fig. 3. Fig. 3(a) shows the effect of porosity on the fluid phase Nusselt number. For relatively

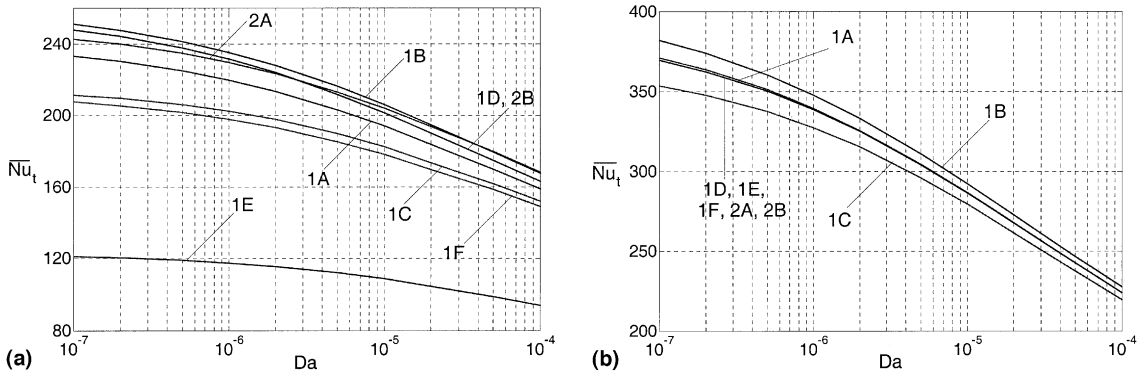

Fig. 6. Effect of Darcy number "Da" on the total Nusselt number excluding the effects of variable porosity and thermal dispersion. (a) $\varepsilon = 0.9$, $Re_p = 100$, $\Lambda = 10$, $d_p = 0.008$, $\kappa = 23.75$. (b) $\varepsilon = 0.5$, $Re_p = 100$, $\Lambda = 10$, $d_p = 0.008$, $\kappa = 1.0$.

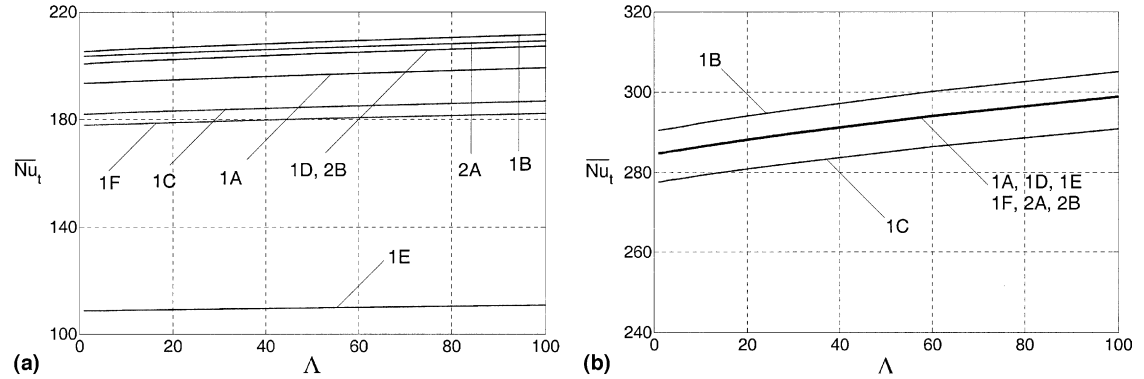

Fig. 7. Effect of the Inertia parameter "Λ" on the total Nusselt number excluding the effects of variable porosity and thermal dispersion. (a) $\varepsilon = 0.9$, $Re_p = 100$, $Da = 10^{-5}$, $d_p = 0.008$, $\kappa = 23.75$. (b) $\varepsilon = 0.5$, $Re_p = 100$, $Da = 10^{-5}$, $d_p = 0.008$, $\kappa = 1.0$.

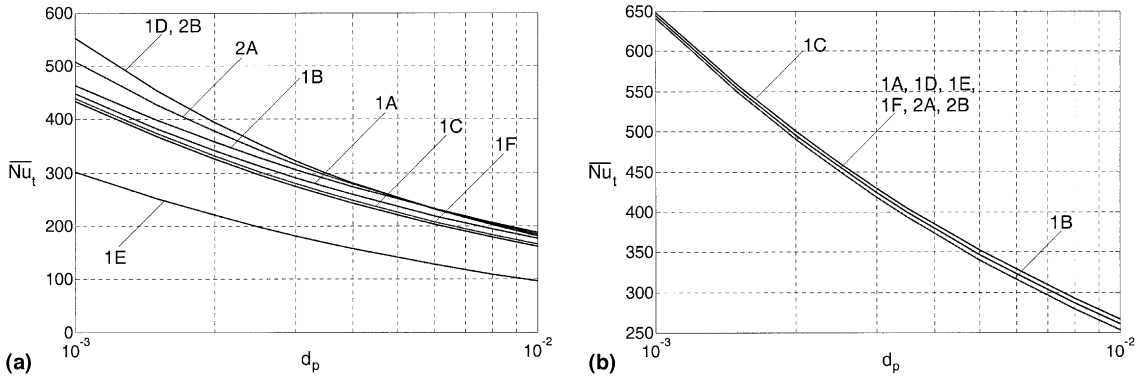

Fig. 8. Effect of the particle diameter "d_p" on the total Nusslet number excluding the effects of variable porosity and thermal dispersion. (a) $\varepsilon = 0.9$, $Re_p = 100$, $Da = 10^{-5}$, $\Lambda = 10$, $\kappa = 23.75$. (b) $\varepsilon = 0.5$, $Re_p = 100$, $Da = 10^{-5}$, $\Lambda = 10$, $\kappa = 1.0$.

small porosities, models 1A, 1B, 1C, 1E and 1F compose a regime of lower Nusselt number values while models 2A and 2B form another regime of higher Nusselt number values. Models 1A, 1B, 1F and 2B converge to the same limit for very high porosities. In addition, models 2A and 1C are close to these models although they do not approach the same limit. On the other hand, model 1E diverges from all the other models for very high porosities. Fig. 3 and Table 2 show that

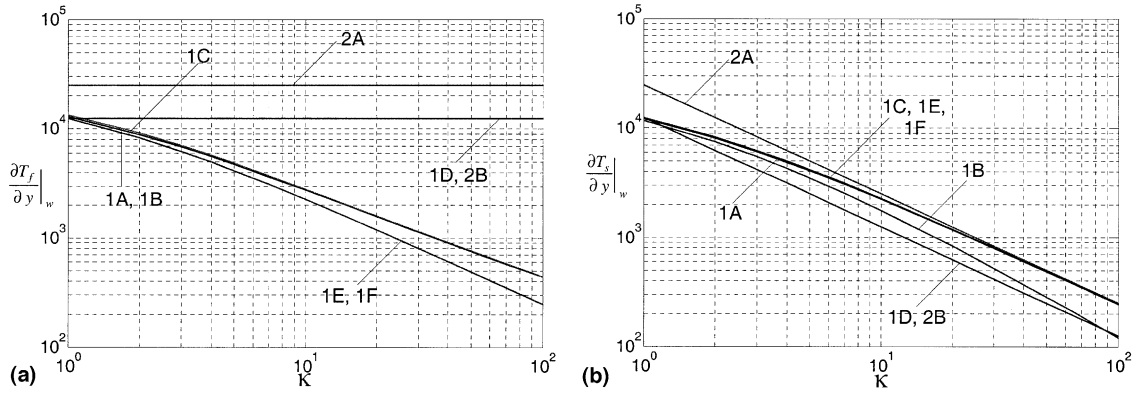

Fig. 9. Effect of the solid-to-fluid conductivity ratio "κ" on the temperature gradients. $\varepsilon = 0.5$, $Re_p = 100$, $Da = 10^{-5}$, $\Lambda = 10$, $d_p = 0.008$. (a) Fluid phase. (b) Solid phase.

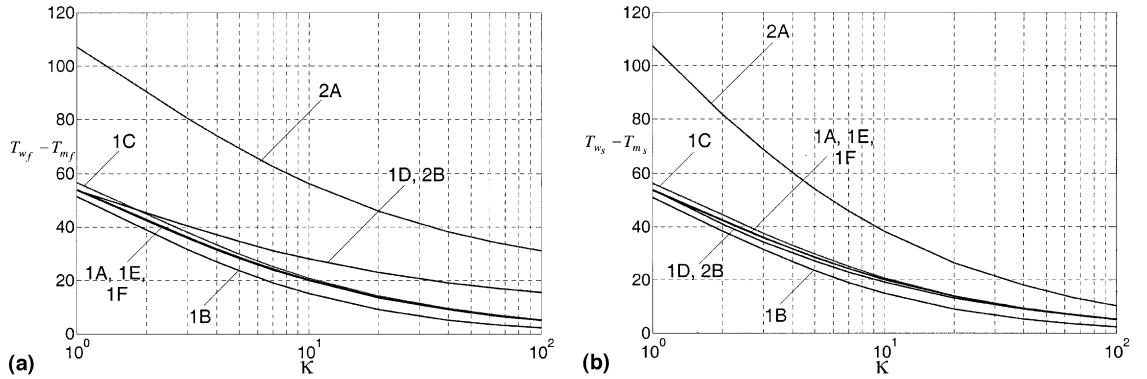

Fig. 10. Effect of the solid-to-fluid conductivity ration "κ" on the difference between the wall temperature and the mean temperature. $\varepsilon = 0.5$, $Re_p = 100$, $Da = 10^{-5}$, $\Lambda = 10$, $d_p = 0.008$. (a) Fluid phase. (b) Solid phase.

models 1E and 1F are exactly alike for the special case of $\varepsilon = 0.5$. The same is found in Fig. 3 for models 2A and 2B. However, results of Table 2 suggest that temperature gradients of model 2A are twice those of model 2B for the special case of $\varepsilon = 0.5$. It is clear that models 1A and 1B approach the same limit as the porosity approaches unity. Theoretically, model 1A is the same as model 1C when the porosity approaches zero while it is the same as model 1B when the porosity approaches unity. So, model 1A would fall between models 1B and 1C for moderate porosity values. An increase in the porosity causes the fluid phase Nusselt numbers ($\overline{Nu}_f$) of models 1A, 1B, 1C and 1F to increase while an increase in the porosity results in the opposite effect for models 2A, 2B and 1E. As for the solid phase Nusselt number, Fig. 3(b) shows that small porosities cause models 1A, 1C, 1E, and 1F to converge while large porosities cause the models to diverge except models 1A and 1B where they approach the same limit when the porosity approaches unity. An increase in the porosity causes the solid phase Nusselt numbers ($\overline{Nu}_s$) of all the models to increase except model 2B where $\overline{Nu}_s$ decreases gradually as the porosity increases. Fig. 3(c) demonstrates the effect of porosity on the total Nusselt number. As mentioned earlier, models 2A and 2B still have the intersection when the porosity is 0.5. Again, the same happens for models 1E and 1F. It is clear that models 1A, 1B, 1F, and 2A converge to the same value when the porosity approaches unity. Models 1C and 2B are still relatively close to these models while model 1E is quite apart from all the models. For relatively small porosities, models 1A, 1B, 1C, 1E and 1F compose a regime of lower Nusselt number values while models 2A and 2B form another regime of higher Nusselt number values. Model 1A intersects with model 2A for a porosity value around 0.93. This affirms that the two conventional models may give the same results under some particular circumstances. Generally, the fluid phase Nusselt numbers have higher values than the solid phase Nusselt numbers which makes the total Nusselt numbers more affected by the fluid phase Nusselt numbers. This result can be observed by comparing Figs. 3(a) and (c).

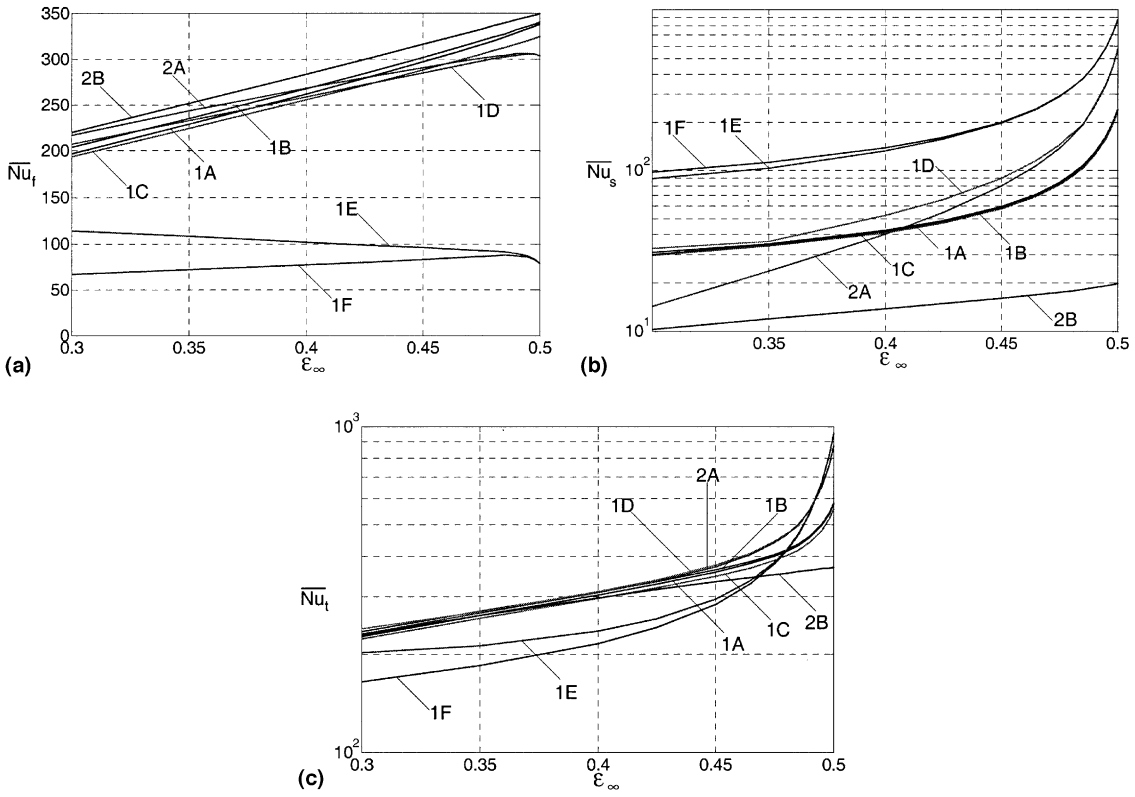

Fig. 11. Effect of the free stream porosity "ε_∞" on the Nusselt number including the effects of variable porosity and thermal dispersion. $b = 0.98$, $c = 2$, $Re_p = 100$, $d_p = 0.008$, $\kappa = 23.75$. Including the effects of variable porosity and thermal dispersion. (a) Fluid phase. (b) Solid phase. (c) Total Nusselt number.

Fig. 4 portrays the effect of the solid-to-fluid conductivity ratio (κ). This ratio κ has a significant impact on the behavior of the represented models. As seen in Fig. 4(a) when the solid-to-fluid conductivity ratio approaches unity, models 1E and 2A converge to the same limit while the other models approach a different limit. On the other hand, $\overline{Nu}_s$ of models 1A, 1B, 1C, 1E, and 1F converge to the same limit for the case of very large values of κ as shown in Fig. 4(b). Some intersections between the models occur in the intermediate range. For example, model 2A intersects with models 1A, 1B, 1C and 1F while there is common point between model 2B and models 1A, 1B and 1C. It is interesting to note that models 2B and 1F are the same when $\kappa = 1$. Temperature gradients of models 1A, 1B, 1C, 1D, 1F and 2B are of the same order of magnitude when $\kappa = 1$ as seen in Table 2.

It is found that all the Nusselt number profiles decrease as the conductivity ratio increases except the fluid phase Nusselt number for model 2A. However, the total Nusselt number of model 2A decreases as κ increases as shown in Fig. 4(c). The numerous intersections of total Nusselt number profiles for different models demonstrate the fact that κ has a substantial impact on these models. Generally, models 1D and 2B form the upper bound for the fluid phase Nusselt number profiles while model 1E forms the lower bound. On the other hand, the opposite is true for the solid phase Nusselt number profiles where model 1E is the upper bound while models 1D and 2B form the lower bound. The total Nusselt number, the summation of $\overline{Nu}_f$ and $\overline{Nu}_s$, provides further insight on the general variances of these models.

Fig. 5 exemplifies the effect of the particle Reynolds number. It is evident from Fig. 5 that an increase in Re_p results in an increase in $\overline{Nu}_t$ for all models. For small values of Re_p, all the models except model 1E are considerably closer to each other as shown in Fig. 5(a). Model 1E has the lowest $\overline{Nu}_t$ while model 1B has the highest $\overline{Nu}_t$. Also, there are no intersections between the models as the value of Re_p changes. Again, the profiles of model 1A falls in between the ones for models 1B and 1C. As shown in Fig. 5(b), models 1A, 1D, 1E, 1F, 2A and 2B coincide when $\varepsilon = 0.5$ and $\kappa = 1$. Models 1B and 1C approach the other models for small values of Re_p where model 1B forms the upper bound and model 1C forms the lower bound. On the other hand, they diverge from the other models as the value of Re_p increases. Table 2 shows that temperature gradients of model 2A are twice those of models 1D, 1E, 1F and 2B for the case ($\varepsilon = 0.5$ and $\kappa = 1$).

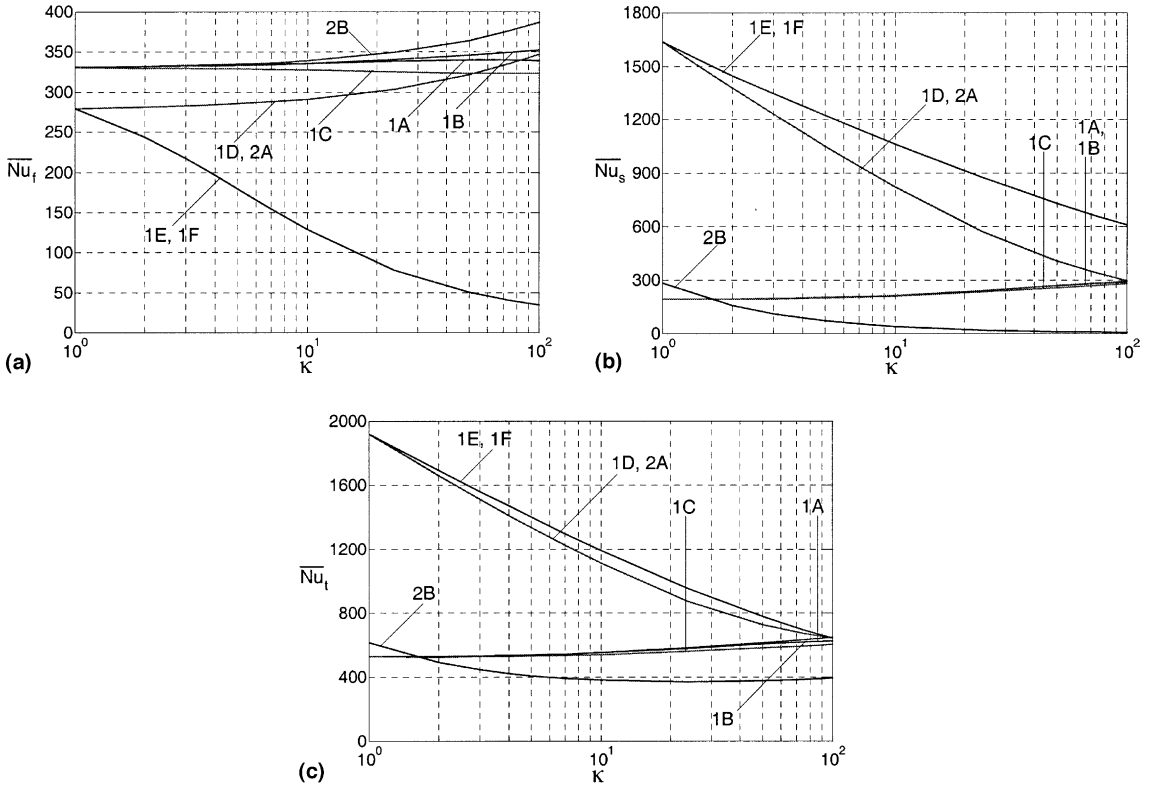

Fig. 12. Effect of the solid-to-fluid conductivity ratio "κ" on the total Nusselt number including the effects of variable porosity and thermal dispersion. $\varepsilon_\infty = 0.5$, $b = 0.98$, $c = 2$, $Re_p = 100$, $d_p = 0.008$ ($\varepsilon_w = 0.99$). Including the effects of variable porosity and thermal dispersion. (a) Fluid phase. (b) Solid phase. (c) Total Nusselt number.

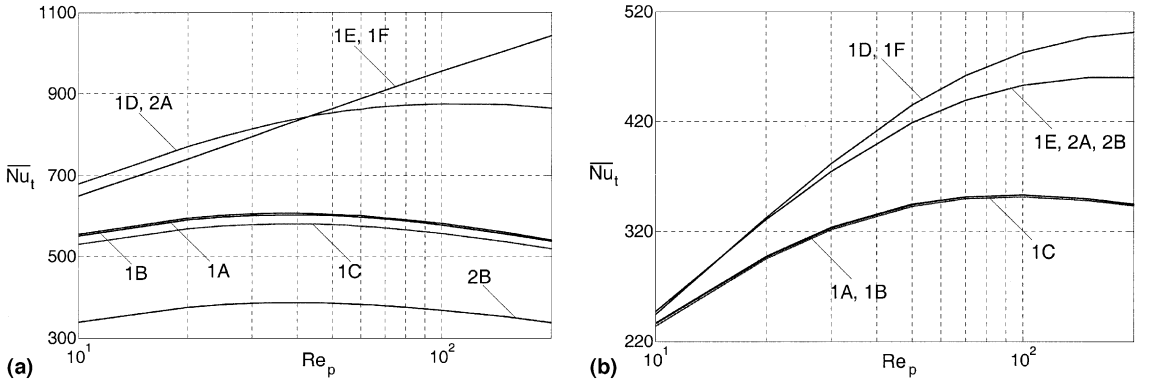

Fig. 13. Effect of the particle Reynolds number "Re_p" on the total Nusselt number including the effects of variable porosity and thermal dispersion. (a) $\varepsilon_\infty = 0.5$, $b = 0.98$, $c = 2$, $d_p = 0.008$, $\kappa = 23.75$ ($\varepsilon_w = 0.99$). (b) $\varepsilon_\infty = 0.4$, $b = 0.25$, $c = 2$, $d_p = 0.008$, $\kappa = 1.0$ ($\varepsilon_w = 0.5$).

At the same time, Fig. 5(b) shows that model 2A is identical to models 1A, 1D, 1E, 1F and 2B. This interesting result regarding model 2A will be discussed later in this section.

Effects of Darcy number on the variant models are depicted in Fig. 6. It is clear that an increase in *Da* leads to a gradual decrease in the $\overline{Nu}_t$ for all models under consideration. Moreover, models 1B and 2A tend to be closer to each other under higher values of *Da*. In fact, they intersect when *Da* is around 4×10^{-4}. Fig. 6(a) shows that once again model 1E is apart from all the other models. However, when the values of the input parameters change as in Fig. 6(b)

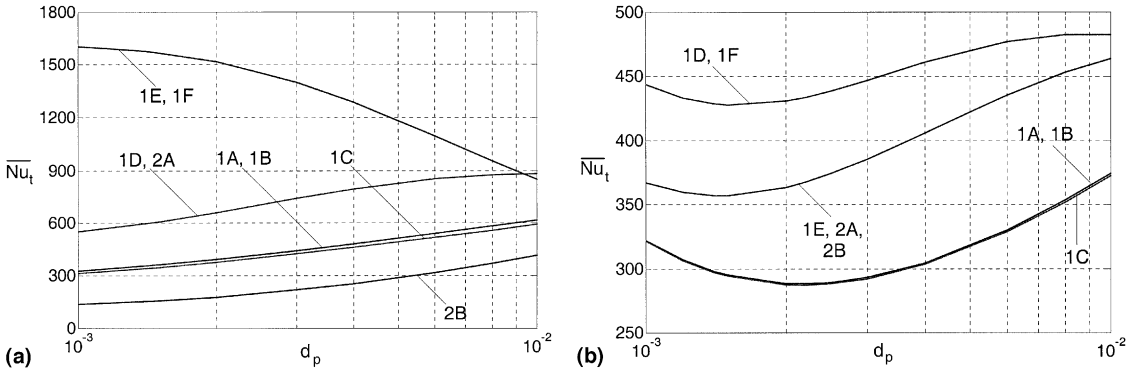

Fig. 14. Effect of the particle diameter "d_p" on the total Nusselt number including the effects of variable porosity and thermal dispersion. (a) $\varepsilon_\infty = 0.5$, $b = 0.98$, $c = 2$, $Re_p = 100$, $\kappa = 23.75$ ($\varepsilon_w = 0.99$). (b) $\varepsilon_\infty = 0.4$, $b = 0.25$, $c = 2$, $Re_p = 100$, $\kappa = 1.0$ ($\varepsilon_w = 0.5$).

Table 2
Mathematical representation of the wall heat flux and the temperature gradients for some special cases

Model	$\kappa = 1$ ($k_s = k_f = k$)	$\varepsilon = 1/2$	$\kappa = 1$ and $\varepsilon = 1/2$
1A	$q_w = -k\left(\varepsilon\frac{\partial T_f}{\partial y} + (1-\varepsilon)\frac{\partial T_s}{\partial y}\right)_{y=0}$	$q_w = -\frac{1}{2}\left(k_f\frac{\partial T_f}{\partial y} + k_s\frac{\partial T_s}{\partial y}\right)_{y=0}$	$q_w = -\frac{k}{2}\left(\frac{\partial T_f}{\partial y} + \frac{\partial T_s}{\partial y}\right)_{y=0}$
1B	$q_w = -k\left(\frac{\partial T_f}{\partial y}\right)_{y=0}$	$q_w = -\frac{k_f + k_s}{2}\left(\frac{\partial T_f}{\partial y}\right)_{y=0}$	$q_w = -k\left(\frac{\partial T_f}{\partial y}\right)_{y=0}$
1C	$q_w = -k\left(\frac{\partial T_s}{\partial y}\right)_{y=0}$	$q_w = -\frac{k_f + k_s}{2}\left(\frac{\partial T_s}{\partial y}\right)_{y=0}$	$q_w = -k\left(\frac{\partial T_s}{\partial y}\right)_{y=0}$
1D	$q_w = -k\left(\frac{\partial T_f}{\partial y}\right)_{y=0} = -k\left(\frac{\partial T_s}{\partial y}\right)_{y=0}$	$q_w = -k_f\left(\frac{\partial T_f}{\partial y}\right)_{y=0} = -k_s\left(\frac{\partial T_s}{\partial y}\right)_{y=0}$	$q_w = -k\left(\frac{\partial T_f}{\partial y}\right)_{y=0} = -k\left(\frac{\partial T_s}{\partial y}\right)_{y=0}$
1E	$q_w = -2\varepsilon k\left(\frac{\partial T_f}{\partial y}\right)_{y=0} = -2(1-\varepsilon)k\left(\frac{\partial T_s}{\partial y}\right)_{y=0}$	$q_w = -\frac{k_f + k_s}{2}\left(\frac{\partial T_f}{\partial y}\right)_{y=0} = -\frac{k_f + k_s}{2}\left(\frac{\partial T_s}{\partial y}\right)_{y=0}$	$q_w = -k\left(\frac{\partial T_f}{\partial y}\right)_{y=0} = -k\left(\frac{\partial T_s}{\partial y}\right)_{y=0}$
1F	$q_w = -k\left(\frac{\partial T_f}{\partial y}\right)_{y=0} = -k\left(\frac{\partial T_s}{\partial y}\right)_{y=0}$	$q_w = -\frac{k_f + k_s}{2}\left(\frac{\partial T_f}{\partial y}\right)_{y=0} = -\frac{k_f + k_s}{2}\left(\frac{\partial T_s}{\partial y}\right)_{y=0}$	$q_w = -k\left(\frac{\partial T_f}{\partial y}\right)_{y=0} = -k\left(\frac{\partial T_s}{\partial y}\right)_{y=0}$
2A	$q_w = -\varepsilon k\left(\frac{\partial T_f}{\partial y}\right)_{y=0} = -(1-\varepsilon)k\left(\frac{\partial T_s}{\partial y}\right)_{y=0}$	$q_w = -\frac{k_f}{2}\left(\frac{\partial T_f}{\partial y}\right)_{y=0} = -\frac{k_s}{2}\left(\frac{\partial T_s}{\partial y}\right)_{y=0}$	$q_w = -\frac{k}{2}\left(\frac{\partial T_f}{\partial y}\right)_{y=0} = -\frac{k}{2}\left(\frac{\partial T_s}{\partial y}\right)_{y=0}$
2B	$q_w = -k\left(\frac{\partial T_f}{\partial y}\right)_{y=0} = -k\left(\frac{\partial T_s}{\partial y}\right)_{y=0}$	$q_w = -k_f\left(\frac{\partial T_f}{\partial y}\right)_{y=0} = -k_s\left(\frac{\partial T_s}{\partial y}\right)_{y=0}$	$q_w = -k\left(\frac{\partial T_f}{\partial y}\right)_{y=0} = -k\left(\frac{\partial T_s}{\partial y}\right)_{y=0}$

model 1E coincides with all the other models except models 1B and 1C. Fig. 6(b) displays similar results to the ones in Fig. 5(b) although model 1A diverges from models 1D, 1E, 1F, 2A and 2B for small values of *Da*. The reason for this behavior is that smaller values of *Da* cause the difference between the fluid and solid temperature gradients of model 1A to increase. This conclusion can be verified from results of models 1B and 1C, which diverge as *Da* decreases. Figs. 6(a) and (b) show that higher values of *Da* decrease the disparity between the variant models under consideration.

Effects of the inertia parameter Λ on all models are shown in Fig. 7. Although the Nusselt numbers of all models exhibit a slight increase as Λ increases, it is found that the effect of Λ is insignificant on $\overline{Nu}_t$ for all the listed models in Table 1. The total Nusselt number profiles are found to have an almost linear relationship with the inertia parameter Λ. Once again, model 1E is apart from other models and model 1A is sandwiched between models 1B and 1C.

Fig. 8 shows the effect of the particle diameter on $\overline{Nu}_t$. In general, an increase in the particle diameter d_p results in a decrease in $\overline{Nu}_t$ for all the models and an increase in d_p attains a convergence between models 1B, 2A and 2B. Again, model 1E has the lowest $\overline{Nu}_t$ while model 2B has the highest $\overline{Nu}_t$. When the porosity is constant and the thermal dispersion effects are omitted, the particle diameter only affects h_{sf} and a_{sf}. For the case of Fig. 8(a), higher values of d_p cause all the models except 1E to converge while for the case of Fig. 8(b), smaller values result in convergence among all models.

It is worth noting that results obtained based on model 2A are of the same order as other models. Although the temperature gradients of model 2A are twice the values of other models for the case of ($\varepsilon = 0.5$ and $\kappa = 1$) as shown in Table 2, its Nusselt number is exactly the same as others when ($\varepsilon = 0.5$ and $\kappa = 1$) as shown in Figs. 5–8. Reviewing the definition of the Nusselt number (Eqs. (14) and (15)) explains this phenomenon. In fact, it is evident that the difference between the wall temperature and the mean temperature for model 2A is twice that of the other models. Fig. 9 demonstrates the effect of κ on the temperature gradients while Fig. 10 displays the effect of κ on the difference between the wall temperature and the mean temperature. Although $\overline{Nu}_t$ of model 2A is of the same order of magnitude as the total Nusselt number of other models, its wall temperature and its temperature gradients reach much greater values than other models. It is clear that the order of magnitude of the temperature gradients of model 2A is nearly twice that obtained from other models for the case ($\kappa = 1$). The same is true for the temperature difference between the wall temperature and the mean temperature. As κ varies, results of the ratio of the temperature gradient to the temperature difference of model 2A and other models change accordingly. Therefore, the Nusselt number of model 2A is of the same order of magnitude as the other models.

At this point, it is found that relating other models to a reference model is desirable. However, designating one model over the others is not an easy issue since some previous studies validated each of the two primary models. In addition to that, the mechanics of splitting the heat flux between the two phases is not yet resolved. Moreover, it is expected that various effects might cause a set of experimental results to agree with one model over the others. These effects include the variable porosity, the thermal dispersion and the wall thickness. It is known that when the wall boundary has a finite thickness composed of a high conductivity material, the two phases should have the same wall temperature. Therefore, for this class of applications, model 1A is preferable. On the other hand, model 2A is anticipated to be a good representative boundary condition for applications with high wall temperatures and high temperature gradients. Fig. 9 shows that fluid phase and solid phase temperature gradients of model 2A are the highest among all models under consideration. In addition, results of Fig. 10 show that solid and fluid wall temperatures of model 2A are the highest among all models under consideration. The results in this work indicate that depending on the application area either model 1A or model 2A will be a better representative boundary condition. Following is a set of correlations that relate other models to model 2A:

$$(\overline{Nu}_t)_{1A} = \left[\frac{3.67 + 2.45\varepsilon^{2.55}}{0.446 + 0.1\varepsilon^{3.55}} - \frac{10.56 + 0.35(\kappa/23.75)}{1.48 + 9.2(\kappa/23.75)^{-5.7} \times 10^{-9}} + 4.04\left(\frac{Re_p}{100}\right)^{0.1} - 0.44\left(Da \times 10^5\right)^{0.18} - 3.94\left(\frac{d_p}{0.008}\right)^{0.1} + 0.51\left(\frac{\Lambda}{100}\right)^{0.02}\right](\overline{Nu}_t)_{2A}^{0.75}, \tag{22}$$

$$(\overline{Nu}_t)_{1B} = \left[\frac{3.87 + 1.782\varepsilon^{1.55}}{0.435 + 0.021\varepsilon^{46.4}} - \frac{21.39 + 0.38(\kappa/23.75)^{1.32}}{2.886 + 1.7(\kappa/23.75)^{-5.79} \times 10^{-8}} + 5.18\left(\frac{Re_p}{100}\right)^{0.12} - 0.87\left(Da \times 10^5\right)^{0.16} - 4.72\left(\frac{d_p}{0.008}\right)^{0.13} + 0.249\left(\frac{\Lambda}{10}\right)^{0.062}\right](\overline{Nu}_t)_{2A}^{0.71}, \tag{23}$$

$$(\overline{Nu}_t)_{1C} = \left[\frac{3.4 + 0.205\varepsilon^{1.83}}{0.455 + 0.0056\varepsilon^{27.43}} - \frac{27.89 + 7.15(\kappa/23.75)^{-4.69} \times 10^{-5}}{3.73 + 6.79(\kappa/23.75)^{-4.81} \times 10^{-6}} + 0.164\left(\frac{Re_p}{100}\right)^{-0.14} - 3.02\left(Da \times 10^5\right)^{-0.0018} - 0.275\left(\frac{d_p}{0.008}\right)^{-0.076} + 3.196\left(\frac{\Lambda}{10}\right)^{-1.94\times10^{-4}}\right](\overline{Nu}_t)_{2A}^{1.13}, \tag{24}$$

$$(\overline{Nu_t})_{1D,2B} = \Bigg[9.253 - 4.309\varepsilon^{5.37} + 2.204\,\mathrm{EXP}(1.829 + 0.09\varepsilon) - 8.537\left(\frac{\kappa}{23.75}\right)^{-0.019} + 2.102\,\mathrm{EXP}\left(2.197 + 3.64\left[\frac{\kappa}{23.75}\right] \times 10^{-3}\right) + 6.937\left(\frac{Re_p}{100}\right)^{0.21} + 26.48\left(Da \times 10^5\right)^{-0.01} - 57.06\left(\frac{d_p}{0.008}\right)^{0.04} + 0.016\left(\frac{\Lambda}{10}\right)^{1.26}\Bigg](\overline{Nu_t})_{2A}^{0.59}, \tag{25}$$

$$(\overline{Nu_t})_{1E} = \Bigg[-6.915 - 4.096\varepsilon^{0.004} + 0.052\,\mathrm{EXP}(-1.891 + 4.876\varepsilon) - 5.37\left(\frac{\kappa}{23.75}\right)^{0.25} + 2.688\,\mathrm{EXP}\left(2.292 + 0.017\left[\frac{\kappa}{23.75}\right]\right) + 2.688\left(\frac{Re_p}{100}\right)^{0.1} - 0.355\left(Da \times 10^5\right)^{0.13} - 11.83\left(\frac{d_p}{0.008}\right)^{0.033} + 0.0027\left(\frac{\Lambda}{10}\right)^{1.19}\Bigg](\overline{Nu_t})_{2A}^{0.76}, \tag{26}$$

$$(\overline{Nu_t})_{1F} = \Bigg[\left(\frac{9.68 \times 10^{-3} + 0.433\varepsilon^{2.9}}{27.116 + 1.82 \times 10^{-4}\varepsilon^{-11.39}}\right) \times \left(\frac{6119.63}{27.69 + 6.984(\kappa/23.75)^{1.27}}\right) + 12.866 \times \left(\frac{Re_p}{100}\right)^{0.023} - 0.225\left(Da \times 10^5\right)^{0.24} - 23.512\left(\frac{d_p}{0.008}\right)^{0.014} + 11.651\left(\frac{\Lambda}{10}\right)^{0.0005}\Bigg](\overline{Nu_t})_{2A}^{0.77}. \tag{27}$$

Limiting cases where models under consideration converge or diverge can be obtained by combining the results of Figs. 3–8. As mentioned earlier, the inertia parameter effect is insignificant on the convergence or divergence of the models. In addition, effect of the particle diameter is found to be vacillating since it depends on the choice of other parameters as shown in Fig. 8. Generally, a porosity value of 0.5, a solid-to-fluid conductivity ratio of unity, low particle Reynolds number values and high Darcy number values cause the models to converge. On the other hand, low porosity values, high solid-to-fluid conductivity ratios, high particle Reynolds number values and small Darcy number values cause the models to diverge.

4.2. Variable porosity, thermal dispersion

Introducing only the effect of thermal dispersion would affect the problem under consideration implicitly since the effective conductivities remain constant at the wall. Therefore, expressions of Tables 1 and 2 are still valid and the results would be analogous to the ones from the Section 4.1. On the other hand, introducing the effect of variable porosity would affect the models in Tables 1 and 2 implicitly as well as explicitly. Models 1D and 1F are greatly affected by the porosity variation since they have a direct dependence on it as shown in Table 1. As a result, model 1D is no longer identical to model 2B when the porosity variations are taken into account. Also, characteristics of model 1F are totally different when effects of variable porosity are included. Consequently, results of Table 2 are valid for all the models except models 1D and 1F. When variable porosity is considered, the three parameters Darcy number, particle diameter and free stream porosity (ε_∞) are linked through Eq. (12). Therefore, analyzing two of these three parameters is sufficient. As a result, effects of the free stream porosity and the particle diameter are considered in this section. Effect of the free stream porosity is shown in Fig. 11. It is evident that the Nusselt numbers for models 1E and 1F are relatively apart from other models. Although models 1D and 1E approach the same limit as the free stream porosity approaches 0.5, they are quite different as porosity decreases. Likewise, models 1A, 1B and 1C are close to each other when the free stream porosity is 0.5 however, they produce values which are also not far from each other for smaller values of the free stream porosity. Moreover, models 1D and 2A approach the same limit when ε_∞ approaches 0.5.

The presented figures are indicative of the general qualitative trend of the results. Effect of the free stream porosity on the solid phase Nusselt numbers is shown in Fig. 11(b). It can be observed that the presented eight models can be categorized into four groups, the first is models 1A, 1B and 1C, the second is 1D and 2A, the third is 1E and 1F, and the forth is model 2B. Remarkable results are projected in Fig. 11(c), it is found that models 1A, 1B, 1C, 1D, 2A, and 2B are very close to each other when low free stream porosity values are considered. Also, models 1D, 1E, 1F and 2A approach the same limit as ε_∞ approaches 0.5. It is important to notice that model 1D becomes identical to model 2A when ε_∞ has a value of 0.5.

Effects of the solid-to-fluid conductivity ratio are shown in Fig. 12. It is found in Fig. 12(a) that when $\kappa = 1$, fluid phase Nusselt numbers for models 1A, 1B, 1C and 2B are almost the same. The same is true for models 1D, 1E, 1F and 2A. For high values of κ, models 1E and 1F diverge from the other models. In Fig. 12, models 1D and 2A are identical because a free stream porosity value of 0.5 is used in this figure. Models 1D and 2A diverge from models 1E and 1F at low values and approach other models as κ increases. As a result, they intersect with models 1A and 1C. Fig. 12(b) shows the results of the solid phase Nusselt numbers. It is found that $\overline{Nu}_s$ values are relatively higher than $\overline{Nu}_f$. Solid phase Nusselt numbers of models 1A, 1B and 1C are found to be close to each other especially for lower κ values. Again, models 1D and 2A separate from models 1E and 1F at small κ values and approach the other models as the value of κ increases. Model 2B essentially provides the lower bound for small $\overline{Nu}_s$ especially for larger values of κ. Generally, results of Fig. 12(c) are equivalent to the ones of Fig. 12(b) because of the higher values of $\overline{Nu}_s$. However, all the models except model 2B converge to the same limit for high values of κ.

In this section, the free stream porosity (ε_∞) as well as the porosity at the wall (ε_w) are found to affect convergence or divergence of the models under consideration. Therefore, choosing appropriate values of the free stream porosity and the parameter b would give a chance to generate a value of 0.5 for the porosity at the wall. This might be achieved by choosing a value of 0.25 for the parameter b along with a free stream porosity value of 0.4. It is observed that choosing a value of unity for κ besides a wall porosity value of 0.5 makes models 1D and 1F identical. The same is true for models 1E, 2A and 2B. Effects of the particle Reynolds number on the total Nusselt numbers $\overline{Nu}_t$ are displayed in Fig. 13. Fig. 13(a) shows that models 1D and 2A are exactly the same when free stream porosity equals 0.5, which is consistent with the results of Fig. 11. The same results are observed for models 1E and 1F. When the particle Reynolds number has a value around 45, the curve of models 1D and 2A intersects with the curve of models 1E and 1F. Models 1D, 2A, 1E and 1F yield the highest values of the total Nusselt number as Re_p varies. It is also found that models 1A and 1B are very close for all values of Re_p. Model 1C is still close to models 1A and 1B. Fig. 13(b) shows the effect Re_p of for the special case of a wall porosity value of 0.5. Unlike results of Fig. 13(a), all the models experience an increase in their $\overline{Nu}_t$ values as the value of Re_p increases. It is observed that models 1D and 1F form the upper bound while models 1A, 1B and 1C form the lower limit. Models 1E, 2A and 2B come in the middle between the previous two sets.

Fig. 14 shows the effects of the particle diameter on the total Nusselt. It is clear that models 1E and 1F produce results that are quite different from the other models. According to Fig. 14(a), the total Nusselt numbers of models 1E and 1F decrease as the particle diameter d_p increases while all the other models experience a slight increase as d_p increases. Model 1C is quite close to models 1A and 1B, which are very close to each other. Results of models 1E and 1F approach the ones of 1D and 2A as d_p increases. Generally, model 2B forms the lower bound while models 1E and 1F form the upper bound for the total Nusselt number profiles in Fig. 14(a). Fig. 14(b) shows the results for the special case of a wall porosity value of 0.5. Three regimes similar to the ones of Fig. 13(b) are found in Fig. 14(b). However, the behavior of the three regimes in Fig. 14(b) is different and more involved. In fact, the behavior of the models in Fig. 14(b) is quite complex where the $\overline{Nu}_t$ profiles of all the three regimes have local minimum values, which are different from one regime to another. The reason behind this behavior is the dependency of several parameters on d_p such as the h_{sf}, a_{sf}, the effective conductivities, the porosity and the permeability. Useful correlations that relate other models to model 2A and the pertinent parameters of this section are listed below:

$$(\overline{Nu}_t)_{1A} = \left[8.56 - 20.205(\varepsilon_\infty[1+b])^{13.89} - 0.494\,\mathrm{EXP}\left(2.541 + 0.065\left[\frac{\kappa}{23.75}\right]\right) - 1.218\left(\frac{Re_p}{100}\right)^{0.16} + \left(1.22(\varepsilon_\infty + 0.557)^{27.97} + 0.657\left[\frac{\kappa}{23.75}\right]^{0.56}\right) \times \mathrm{EXP}\left(1.078 + 0.047\left[\frac{d_p}{0.008}\right]\right) - 0.064\left(\frac{d_p}{0.008}\right)\right](\overline{Nu}_t)_{2A}^{0.81}, \tag{28}$$

$$(\overline{Nu}_t)_{1B} = \left[8.01 - 19.44(\varepsilon_\infty[1+b])^{14.03} - 0.22\,\mathrm{EXP}\left(3.214 + 0.068\left[\frac{\kappa}{23.75}\right]\right) - 1.298\left(\frac{Re_p}{100}\right)^{0.15} + \left(1.25(\varepsilon_\infty + 0.553)^{28.18} + 0.639\left[\frac{\kappa}{23.75}\right]^{0.56}\right) \times \mathrm{EXP}\left(1.093 + 0.047\left[\frac{d_p}{0.008}\right]\right) - 0.061\left(\frac{d_p}{0.008}\right)\right](\overline{Nu}_t)_{2A}^{0.81}, \tag{29}$$

$$(\overline{Nu_t})_{1C} = \left[8.79 - 21.35(\varepsilon_\infty[1+b])^{13.81} - 1.52\,\mathrm{EXP}\left(1.453 + 0.056\left[\frac{\kappa}{23.75}\right]\right) - 1.116\left(\frac{Re_p}{100}\right)^{0.19} + \left(1.27(\varepsilon_\infty + 0.557)^{27.89} + 0.65\left[\frac{\kappa}{23.75}\right]^{0.53}\right) \times \mathrm{EXP}\left(1.098 + 0.055\left[\frac{d_p}{0.008}\right]\right) - 0.089\left(\frac{d_p}{0.008}\right)\right](\overline{Nu_t})_{2A}^{0.8}, \tag{30}$$

$$(\overline{Nu_t})_{1D} = \left[1.535 - (0.464 + 0.11[1+b]\varepsilon_\infty) + 6.51\,\mathrm{EXP}\left(-4.297 + 0.132\left[\frac{\kappa}{23.75}\right]\right) \times 10^{-3} + 0.048\left(\frac{Re_p}{100}\right)^{-0.48} + \left(4.31\varepsilon_\infty^{0.022} - 0.725\left[\frac{\kappa}{23.75}\right]^{-0.019}\right) \times \left[\mathrm{EXP}\left(0.474 - 1.573\left[\frac{d_p}{0.008}\right]\right) + 0.856\left(\frac{d_p}{0.008}\right)\right]\right](\overline{Nu_t})_{2A}, \tag{31}$$

$$(\overline{Nu_t})_{1E} = \left[-1.322 - 0.108(3.759 + 5.176[1+b]\varepsilon_\infty)^{-765.04} + 0.801\,\mathrm{EXP}\left(1.19 - 0.171\left[\frac{\kappa}{23.75}\right]\right) - 0.345\left(\frac{Re_p}{100}\right)^{0.58} + (-1.106 + 2.339[1+b]\varepsilon_\infty)^{12.28} \times \left(0.128 + \left[\frac{\kappa}{23.75}\right]\right)^{0.58} \times \left(1.25 + \left[\frac{d_p}{0.008}\right]\right)^{-3.53}\right](\overline{Nu_t})_{2A}^{0.92}, \tag{32}$$

$$(\overline{Nu_t})_{1F} = \left[-15.71 - 21.23([1+b]\varepsilon_\infty)^{0.042} + 1.752\,\mathrm{EXP}\left(3.05 - 0.039\left[\frac{\kappa}{23.75}\right]\right) + 0.131\left(\frac{Re_p}{100}\right)^{0.71} + \left(2.89\varepsilon_\infty^{6.94} + 0.056\left[\frac{\kappa}{23.75}\right]^{0.91}\right) \times \left[\mathrm{EXP}\left(2.896 - 2.908\left[\frac{d_p}{0.008}\right]\right) + 26.555\left(\frac{d_p}{0.008}\right)^{-0.11}\right]\right](\overline{Nu_t})_{2A}^{1.036}, \tag{33}$$

$$(\overline{Nu_t})_{2B} = \left[0.767 - 8.627([1+b]\varepsilon_\infty)^{21.15} + 0.206\,\mathrm{EXP}\left(-0.741 + 0.587\left[\frac{\kappa}{23.75}\right]\right) - 0.481\left(\frac{Re_p}{100}\right)^{0.037} + \left(5092.94\varepsilon_\infty^{21.09} - 5.05 \times 10^{-6}\left[\frac{\kappa}{23.75}\right]^{2.87}\right) \times \left[\mathrm{EXP}\left(7.972 + 0.042\left[\frac{d_p}{0.008}\right]\right) - 92.767\left(\frac{d_p}{0.008}\right)\right]\right](\overline{Nu_t})_{2A}^{1.13}. \tag{34}$$

There is no universal situation where the eight models converge or diverge from each other when variable porosity effects are taken into account. However, it is found that low free stream porosity, high solid-to-fluid conductivity ratio and low particle Reynolds number cause models 1A, 1B, 1C, 1D and 2A to converge. Since many parameters depend on the particle diameter, its effect on the convergence and divergence of the models is significantly dependent on the choice of other parameters.

5. Conclusion

A comprehensive investigation of variant boundary conditions for constant wall heat flux in porous media under LTNE conditions has been presented in this work. It is evident that using different boundary conditions may lead to substantially different results. Physical properties are found to have a significant impact on the heat transfer predictions using the models listed in Table 1. Generally, models 1A and 1B are relatively close to each other while models 1C and

2B are exactly the same when thermal dispersion effects are excluded. Effects of porosity, particle Reynolds number, Darcy number, particle diameter and solid-to-fluid conductivity ratio are found to be significant when variable porosity and thermal dispersion effects are excluded. Effects of inertia parameter are found to be relatively insignificant on $\overline{Nu}_f$, $\overline{Nu}_s$ and $\overline{Nu}_t$. In general, model 1E forms the lower bound while model 2B forms the upper bound for $\overline{Nu}_f$. On the other hand, model 1E form the upper bound while model 2B forms the lower bound for $\overline{Nu}_s$. Including the effects of variable porosity and thermal dispersion altered the sequence of the models in terms of their $\overline{Nu}_f$, $\overline{Nu}_s$ and $\overline{Nu}_t$ predictions. Including these effects causes intermediacy independence between some of the pertinent parameters. Special cases when variant models under consideration converge are obtained. Comprehensive sets of correlation that relate various models to each other in terms of the total Nusselt number are presented.

References

[1] A. Amiri, K. Vafai, T.M. Kuzay, Effects of boundary conditions on non-Darcian heat transfer through porous media and experimental comparisons, Numer. Heat Transfer, Part A 27 (1995) 651–664.

[2] G.J. Hwang, C.C. Wu, C.H. Chao, Investigation of non-Darcian forced convection in an asymmetrically heated sintered porous channel, J. Heat Transfer 117 (1995) 725–732.

[3] D.L. Lee, K. Vafai, Analytical characterization and conceptual assessment of solid and fluid temperature differentials in porous media, Int. J. Heat Mass Transfer 42 (1999) 423–435.

[4] D. Kim, S.J. Kim, Thermal interaction at the interface between a porous medium and an impermeable wall, presented at the 4th KSME-JSME Thermal Engineering Conference, Kobe, Japan, October 1–6, 2000.

[5] G.J. Hwang, C.H. Chao, Heat transfer measurement and analysis for sintered porous channels, J. Heat Transfer 116 (1994) 456–464.

[6] D.A. Nield, Effects of local thermal nonequilibrium in steady convective processes in a saturated porous medium: Forced convection in a channel, J. Porous Media 1 (1998) 181–186.

[7] D.A. Nield, A.V. Kuznetsov, Local thermal nonequilibrium effects in forced convection in a porous medium channel: a conjugate problem, Int. J. Heat Mass Transfer 42 (1999) 3245–3252.

[8] A.V. Kuznetsov, Thermal nonequilibrium, non-Darcian forced convection in a channel filled with a fluid saturated porous medium – a perturbation solution, Appl. Sci. Res. 57 (1997) 119–131.

[9] V.V. Calmidi, R.L. Mahajan, Forced convection in high porosity metal foams, J. Heat Transfer 122 (2000) 557–565.

[10] A.R. Martin, C. Saltiel, W. Shyy, Heat transfer enhancement with porous inserts in recirculating flows, J. Heat Transfer 120 (1998) 458–467.

[11] P.X. Jiang, Z.P. Ren, Numerical investigation of forced convection heat transfer in porous media using a thermal non-equilibrium model, Int. J. Heat Fluid Flow 22 (2001) 102–110.

[12] P.X. Jiang, Z.P. Ren, B.X. Wang, Experimental research of fluid flow and convection heat transfer in plate channels filled with glass or metallic particles, Exp. Thermal Fluid Sci. 20 (1999) 45–54.

[13] P.X. Jiang, Z.P. Ren, B.X. Wang, Numerical simulation of forced convection heat transfer in porous plate channels using thermal equilibrium and nonthermal equilibrium models, Numer. Heat Transfer, Part A 35 (1999) 99–113.

[14] P.X. Jiang, Z.P. Ren, B.X. Wang, Z. Wang, Forced convective heat transfer in a plate channel filled with solid particles, J. Thermal Sci. 5 (1996) 43–53.

[15] K. Ichimiya, T. Matsuda, Y. Kawai, Effects of a porous medium on local heat transfer and fluid flow in a forced convection field, Int. J. Heat Mass Transfer 40 (1997) 1567–1576.

[16] A. Mahmid, S. Ben Nasrallah, J.P. Fohr, Heat and mass transfer during drying of granular products simulation with convective and conductive boundary conditions, Int. J. Heat Mass Transfer 43 (2000) 2779–2791.

[17] A. Amiri, K. Vafai, Analysis of dispersion effects and non-thermal equilibrium, non-Darcian, variable porosity incompressible flow through porous media, Int. J. Heat Mass Transfer 37 (1994) 939–954.

[18] K. Vafai, Heat transfer in variable porosity media, J. Fluid Mech. 147 (1984) 233–259.

[19] K. Vafai, S.J. Kim, Forced convection in a channel filled with a porous medium: an exact solution, J. Heat Transfer 111 (1989) 1103–1106.